Research Square

Preprints are preliminary reports that have not undergone peer review.
They should not be considered conclusive, used to inform clinical practice,
or referenced by the media as validated information.

# Mapping post-translational modifications across amyloid-β deposits in Alzheimer's disease: A neuropathologic survey with in vitro functional analysis of nitration

**Sarah Basile**
University of Catania
**Fleur Schipper**
Amsterdam UMC location VUmc
**Stefania Zimbone**
National Research Council
**Sanne M.M. Vermorgen**
Amsterdam UMC location VUmc
**Francesco Bellia**
University of Catania
**Cristina Parisi**
University of Catania
**Salvatore Sortino**
University of Catania
**Jochen Walter**
University of Bonn
**Maria Laura Giuffrida**
National Research Council
**Annemiek J.M. Rozemuller**
Amsterdam UMC location VUmc
**Jeroen J.M. Hoozemans**
Amsterdam UMC location VUmc
**Agata Copani**
University of Catania
**Baayla D.C. Boon**
boon.baayla@mayo.edu

Mayo Clinic in Florida

**Research Article**

**Keywords:** Amyloid-β, Post-translational modifications, 3-Nitrotyrosine, Cerebral amyloid angiopathy, Nitration, Phosphorylation, Pyroglutamylation, Alzheimer's disease

**Posted Date:** October 18th, 2026

**DOI:** https://doi.org/10.21203/rs.3.rs-10769225/v1

**License:** This work is licensed under a Creative Commons Attribution 4.0 International License. Read Full License

**Additional Declarations:** Competing interest reported. FS, SZ, SMMV, FB, CP, SS, JW, MLG, AJMR declare they have no competing interests. SB has received travel support to attend scientific meetings. JJMH is employed by F. Hoffmann-La Roche. AC reports no conflicts of interest. BDCB receives research support from Alzheimer Nederland, the BrightFocus Foundation, and the Mayo Clinic Alzheimer's Disease Research Center. She has received honoraria from F. Hoffmann-La Roche and travel support to attend scientific meetings.

## Abstract

# Background

Amyloid-β (Aβ) pathology in Alzheimer's disease (AD) includes distinct types of plaques and cerebral amyloid angiopathy (CAA). Post-translational modifications (PTMs) may define Aβ deposit-specific signatures. Among them, nitration of tyrosine-10 (3'-nitrotyrosine, 3-NT) links oxidative stress to Aβ modification and microglial activation, but its spatial distribution across deposit types and impact on aggregation dynamics remain unclear.

# Methods

Parietal cortex tissue from AD and CAA cases (n = 19) and controls (n = 9) was analyzed by multiplex immunofluorescence for Aβ species (Aβaa1-8, AβN3pE, pSer8-Aβ), 3-NT, thioflavin-S, and CD68. Distinct deposits, including diffuse plaques (n = 70) classic cored plaques (n = 70), coarse-grained plaques (n = 40), capillary CAA (capCAA; n = 80), larger vessel CAA (n = 80), and leptomeningeal CAA (n = 25) were annotated, together with gray matter regions from control tissue lacking Aβ pathology (n = 90). In vitro assays evaluated how 3-NT affects Aβ aggregation kinetics, microglial morphology, and neuronal viability.

# Results

We observed Aβ deposit-specific PTM signatures. Classic cored and coarse-grained plaques contained increased pyroglutamylated ($Aβ_{N3pE}$) and phosphorylated (pSer8-Aβ) species compared to diffuse plaques. In contrast, 3-NT showed a distinct vascular predilection, with the highest relative burden in larger vessel and leptomeningeal CAA. 3-NT colocalized with β-sheet–rich thioflavin-S-positive fibrils and areas of CD68-positive microglia. In vitro, nitration slowed oligomer-to-fibril conversion but accelerated the growth of pre-formed fibrils and sustained microglial activation without increasing neuronal toxicity.

# Conclusions

Distinct PTMs delineate the compartment-specific architectural signatures of Aβ deposits. Whereas AβN3pE and pSer8-Aβ broadly label parenchymal plaques, 3-NT shows a vascular predilection, particularly in leptomeningeal CAA. This compartmentalized pattern identifies nitration as a candidate marker of vascular Aβ pathology and a possible risk indicator for amyloid-related imaging abnormalities (ARIA) during anti-Aβ immunotherapy.

## Background

Alzheimer's disease (AD) is characterized by extracellular amyloid-β (Aβ) deposits and intracellular neurofibrillary tangles of hyperphosphorylated tau protein. Aβ deposition typically precedes that of tau and represents the most extensively validated therapeutic target [1]. Physiologically produced as a monomer possessing physiological functions [2], Aβ can misfold and aggregate into toxic oligomers, protofibrils, and

fibrils that ultimately form deposits in the brain parenchyma as plaques or within cerebral blood vessels as cerebral amyloid angiopathy (CAA) [3].

Aβ deposits, including diffuse plaques, classic cored plaques, coarse-grained plaques, and vascular deposits affecting either capillaries (capCAA), larger parenchymal vessels, or leptomeningeal vessels, are not only morphologically but also pathophysiologically diverse. Although Aβ pathology can be detected in cognitively unimpaired individuals [4–6], certain deposits such as the coarse-grained plaque and capCAA show stronger association with clinical decline, whereas diffuse plaques, classic cored plaques, and larger-vessel CAA often occur without clear clinical consequences [7–11]. Preliminary observations from our recent study suggest that leptomeningeal CAA, more so than capillary or larger-vessel CAA, may be associated with amyloid-related imaging abnormalities (ARIA), although this requires confirmation in larger cohorts [12]. Prior work comparing individual plaque subtypes has revealed differences in fibril structure and neuroinflammatory response [10, 13, 14]. In addition to structural differences, Aβ deposits are also defined by molecular signatures, including isoform composition and post-translational modifications (PTMs), which may further influence aggregation, fibril maturation, glial activation, and disease progression [10, 11, 13, 15]. These include spontaneous molecular aging modifications such as L-isoaspartate formation at Asp7 [16], as well as regulated PTMs including pyroglutamylation and phosphorylation, all of which have been implicated in the maturation and biological properties of Aβ deposits [15, 17]. Despite their distinct implications for disease pathogenesis and therapeutic response, systematic analyses directly contrasting parenchymal and vascular Aβ deposits remain limited.

Neuroinflammation is a crucial component of Aβ pathology [18–20], characterized by activation of microglia and astrocytes surrounding plaques, accompanied by the release of cytokines, chemokines, and nitric oxide [21–23]. Among the downstream effects of nitric oxide, tyrosine nitration at position 10 of Aβ (3'-nitrotyrosine, 3-NT) is of particular interest because it associates nitro-oxidative stress to plaque maturation and glial activation [24, 25]. While nitration has been shown in vitro to divert Aβ aggregation away from canonical fibrils and to modulate microglial responses [26], its distribution across deposit subtypes in human tissue and relationship to other PTMs remains poorly understood. Recognizing the diversity of PTMs in Aβ pathology, we compared nitration alongside two well-characterized PTMs, pyroglutamylation ($Aβ_{N3pE}$) and phosphorylation (pSer8-Aβ), to determine whether nitration represents a general feature of Aβ pathology or a compartment-specific modification across parenchymal and vascular deposits. We then extended these findings in vitro to directly test how nitration influences Aβ fibrillogenesis, microglial activation, and neuronal viability.

## Methods

# Post-mortem human brain tissue

We used brain tissue from individuals with AD and CAA pathology (n = 19) and controls without neurodegenerative disease (n = 9) (Table 1). Seventeen cases fulfilled AD criteria, defined by the clinical syndrome of dementia and a moderate to high level of AD neuropathologic change, while two additional cases were included because of severe CAA pathology despite not meeting criteria for AD neuropathologic change [27]. Brain dissection and neuropathologic diagnosis were performed according to international guidelines of Brain Net Europe II consortium and of the National Institute on Aging-Alzheimer's Association (NIA-AA) [27]. AD neuropathologic change is reported for tangles and Aβ plaques using Braak and Thal staging [28, 29]. Post-

mortem brain tissue was obtained from the Netherlands Brain Bank (NBB), Amsterdam, the Netherlands, and the department of pathology at the Amsterdam UMC, Amsterdam, the Netherlands. In compliance with all ethical standards, brain donors or their next of kin signed informed consent regarding the usage of their brain tissue and clinical records for research purposes. The brain donor program is approved by the medical ethics committee of the Amsterdam UMC. We used fresh-frozen (FF) and formalin-fixed paraffin-embedded (FFPE) tissue from the superior parietal lobule, as this neocortical area shows all Aβ deposits of interest [11, 30–32].

Table 1
Case details.

| Case | Sex | Age of death (yrs) | Braak tangle stage | Thal Aβ phase | Brain weight (g) | *APOE* | Neuropathologic diagnosis |
|---|---|---|---|---|---|---|---|
| 1 | F | 82 | 6 | ≥ 4 | 1010 | 24 | AD |
| 2 | F | 81 | 6 | ≥ 4 | 877 | 33 | AD |
| 3 | F | 81 | 6 | ≥ 4 | 888 | 34 | AD |
| 4 | F | 87 | 6 | ≥ 4 | 1081 | 34 | AD |
| 5 | F | 72 | 6 | ≥ 4 | 960 | 23 | AD |
| 6 | F | 90 | 6 | ≥ 4 | 1018 | 23 | AD |
| 7 | M | 81 | 5 | ≥ 4 | 1191 | 44 | AD with vascular encephalopathy |
| 8 | M | 59 | 6 | ≥ 4 | 1300 | 44 | AD |
| 9 | F | 70 | 6 | ≥ 4 | 894 | 44 | AD |
| 10 | F | 91 | 6 | ≥ 4 | 900 | 34 | AD |
| 11 | M | 59 | 5 | ≥ 4 | 1520 | 33 | AD |
| 12 | M | 68 | 2 | 0 | 1500 | 44 | Vascular dementia with CAA |
| 13 | F | 96 | 5 | ≥ 4 | 1102 | 34 | AD with congophilic angiopathy |
| 14 | M | 88 | 5 | ≥ 4 | 1290 | 44 | AD with congophilic angiopathy |
| 15 | F | 95 | 5 | ≥ 3 | 906 | 44 | AD with vascular encephalopathy |
| 16 | F | 84 | 5 | ≥ 4 | 1004 | 44 | AD with congophilic angiopathy |
| 17 | M | 77 | 5 | 4 | 1006 | 44 | AD with congophilic angiopathy |
| 18 | M | 71 | 1 | 1 | 1215 | N/A | CAA due to HCHWA-D |
| 19 | M | 74 | 5 | 4 | 1230 | N/A | AD with CAA |
| 20 | F | 72 | N/A | N/A | 1300 | N/A | Control |
| 21 | F | 69 | N/A | N/A | 1290 | N/A | Control |

*APOE* genotype is listed as allele combination (e.g., 24 = ε2/ε4). Brain weights represent fresh tissue weight at autopsy. Cases 1–19 represent Alzheimer's disease (AD) and AD with concomitant CAA or vascular pathology, including one hereditary CAA case due to HCHWA-D (case 18). Cases 20–28 served as non-demented controls. AD Alzheimer's disease; CAA cerebral amyloid angiopathy; F female; M male; N/A not available.

| Case | Sex | Age of death (yrs) | Braak tangle stage | Thal Aβ phase | Brain weight (g) | *APOE* | Neuropathologic diagnosis |
|---|---|---|---|---|---|---|---|
| 22 | M | 56 | 0 | 0 | 1548 | 34 | Control |
| 23 | M | 74 | 0 | 0 | 1231 | 33 | Control with ischemic changes |
| 24 | M | 49 | 0 | 0 | 1364 | 23 | Control |
| 25 | M | 90 | 2 | 0 | 1215 | 33 | Control |
| 26 | M | 79 | 2 | 1 | 1121 | 23 | Control |
| 27 | M | 83 | 1 | 1 | 1372 | 33 | Control |
| 28 | M | 89 | 2 | 0 | 1185 | 33 | Control |

*APOE* genotype is listed as allele combination (e.g., 24 = ε2/ε4). Brain weights represent fresh tissue weight at autopsy. Cases 1–19 represent Alzheimer's disease (AD) and AD with concomitant CAA or vascular pathology, including one hereditary CAA case due to HCHWA-D (case 18). Cases 20–28 served as non-demented controls. AD Alzheimer's disease; CAA cerebral amyloid angiopathy; F female; M male; N/A not available.

## Aβ deposit selection

Sections stained for Aβ were scored for distinct deposits (classic cored plaques, coarse-grained plaques, and CAA) using a semi-quantitative score readapted from Boon et al., 2020 [11]. Briefly, deposits were scored from 0 to 3 based on their density per 1 cm²: 0, none; 1, few; 2, moderate; and 3, many. For each case, scores across the evaluated regions were averaged to obtain a representative value for that slide. Cases were then grouped according to the predominant deposit type (**eTable 1 in Additional file 1**), which was subsequently annotated in the corresponding immunofluorescent stainings.

## Immunofluorescence

Multi-label immunofluorescence was performed on 5µm-thick sections. Frozen tissue sections were fixed in acetone for 10 min prior to staining and then triple-stained for $A\beta_{aa1-x}$ + 3-NT+either thioflavin-S or different Aβ species, including $A\beta_{NpE3}$ and pSer-Aβ (Table 2). Thioflavin-S staining was carried out after antibody incubation by submerging slides in 1% thioflavin-S. FFPE sections were double-stained for $A\beta_{aa1-x}$ + CD68. After deparaffinization and dehydration, antigen retrieval for FFPE slides was performed by autoclaving in sodium citrate buffer (pH 6.0, 121°C for 20 minutes). For both frozen and FFPE, primary antibodies were diluted in a ready-to-use antibody dilution buffer with BSA (Sigma-Aldrich, cat# U3510) and incubated overnight. Secondary antibodies were diluted 1:250 in antibody dilution buffer and incubated for 1 hour. All sections underwent a 5-minute incubation with 0,1% Sudan Black in ethanol 70% to quench autofluorescence. Slides stained with thioflavin-S were mounted with a solution of glycerol/TBS 70/30, all other slides with Fluoromount-G™ mounting medium with DAPI (Invitrogen, cat# 00-4959-52,) and coverslipped. In between steps, sections were rinsed in phosphate-buffered solution (pH 7.6). Sections were stored at 4°C until scanning.

Technical control experiments were performed to evaluate tissue autofluorescence, nonspecific secondary-antibody binding, and secondary-antibody cross-reactivity. For negative controls, sections were processed identically except that the primary antibodies were omitted while all secondary antibodies were included. No deposit-associated fluorescence was observed under the acquisition settings used for experimental sections. To assess potential secondary-antibody cross-reactivity within the multiplex immunofluorescence protocol, each primary antibody was stained individually while the complete panel of secondary antibodies was applied. In all cases, fluorescence was detected exclusively in the expected channel, with no detectable signal in the non-corresponding channels.

Table 2
Immunofluorescence antibody characteristics and staining details.

| Antigen | Antibody clone | Source | Host | Isotype | Tissue | Dilution | Secondary step | Threshold for positive pixels |
|---|---|---|---|---|---|---|---|---|
| $A\beta_{aa1-x}$ | IC16[33] | Prof. Dr. Carsten Korth, Heinrich-Heine-Universität Düsseldorf, Germany | Mouse | IgG2a | FFPE | 1:200 | goat-anti-mouse-IgG2a<br>Alexa 488 | 150 |
| | | | | | Frozen | 1:200 | goat-anti-mouse-IgG2a<br>Alexa 488<br>goat-anti-mouse-IgG2a<br>Alexa 647 | 150<br>800 |
| $A\beta_{N3pE}$ | 337.48 | BioLegend | Mouse | IgG1k | Frozen | 1:1600 | goat-anti-mouse-IgG1<br>Alexa 647 | 2000 |
| pSer8-Aβ | 1E4E11[34] | Prof. Dr. Jochen Walter, University Hospital Bonn, Bonn, Germany | Mouse | IgG1k | Frozen | 1:400 | goat-anti-mouse-IgG1<br>Alexa 647 | 1500 |
| 3-NT | HM.11 | Abcam | Mouse | IgG2b | Frozen | 1:25 | goat-anti-mouse-IgG2b<br>Alexa 594 | 120 |
| CD68 | KP1 | Dako | Mouse | IgG1 | FFPE | 1:300 | goat-anti-mouse-IgG1<br>Alexa 647 | 350 |

Overview of all antibodies applied in this study, including antigen target, clone, source, host species, isotype, and working dilution. The table also lists the tissue type used (formalin-fixed paraffin-embedded [FFPE] or frozen) and the corresponding fluorescent secondary antibody.

aa amino-acid; Aβ amyloid-β; FFPE formalin-fixed (4%) paraffin-embedded.

## Antibody specificity and validation

Primary antibodies were selected based on technical validation and established epitope mapping when available:

**$A\beta_{aa1-x}$ (clone IC16)**

Specificity for N-terminally intact Aβ species (epitope aa1–8) has been validated by peptide competition assays, where pre-incubation with synthetic $A\beta aa_{1-16}$ or $A\beta aa_{1-8}$ but not $A\beta aa_{8-15}$ quenched immunoreactivity [35–37].

**AβN3pE (clone 337.48)**

Clone 337.48 was generated against a synthetic pyroglutamate-modified Aβ peptide corresponding to residues 3–16 (manufacturer information). According to the manufacturer's technical validation, ELISA-based binding assays demonstrated selective binding to pyroglutamate-modified Aβ, with no detectable binding to the full-length Aβ or recombinant tau proteins included in the validation panel. These data are consistent with the intended specificity of clone 337.48 for pyroglutamate-modified Aβ species.

**pSer8-Aβ (clone 1E4E11)**

Specificity for Ser8-phosphorylated Aβ was established by Kumar et al. via ELISA, Western blotting, and immunohistochemical competition assays [38]. Clone 1E4E11 specifically recognizes pSer8-Aβ without cross-reacting with non-phosphorylated Aβ, pSer26-Aβ, 3-NT-Aβ, $A\beta_{3-42}$, or $A\beta_{N3pE}$. Immunostaining is completely blocked by pre-incubation with a 200-fold molar excess of synthetic pSer8-Aβ peptide, whereas non-phosphorylated Aβ peptide does not block binding.

**3-NT (clone HM.11)**

Clone HM.11 recognizes 3-nitrotyrosine residues and has been reported by the manufacturer not to cross-react with unmodified tyrosine, phenylalanine, phosphotyrosine, or 3-chlorotyrosine. Because HM.11 recognizes nitrotyrosine independently of the parent protein, its signal is referred to throughout as 3-NT immunoreactivity. Spatial overlap with Aβ-positive deposits indicates enrichment of nitrotyrosine-containing proteins within these deposits.

# Digital pathology

Slides were scanned at 20x magnification on an Olympus Slideview SV200 slide scanner (Olympus Corporation, Tokyo, Japan). Distinct deposit types were annotated in QuPath (version 5.0) using the closed polygon tool in the $A\beta_{aa1-x}$ channel. To prevent bias during annotation, all other channels were switched off. For each case, we annotated 10 deposits representative of the predominant deposit type in the assigned group, along with 5 diffuse plaques (when present). In all CAA cases, 5 leptomeningeal vessels affected by CAA were also annotated when available. For each control case, 10 random Aβ-negative gray matter areas and 3–6 vessels were annotated. The number of deposits annotated per case is described in **eTable 1 in Additional file 1**. Based on qualitative differences between the core and corona of classic cored plaques, we separately annotated these regions in a total of 25 plaques (5 plaques in 5 cases with predominant cored plaque pathology). Annotated deposits were analyzed for percentage of positive pixels using marker dependent thresholds

(Table 2). These thresholds were established based on background fluorescence in target-negative regions and applied uniformly across all images to isolate specific signal. Sections were excluded from analysis if tissue rupture, detachment, or drying artifacts during staining compromised image quality (**eTable 1 in Additional file 1**).

# Aβ assemblies and irradiation setup

We prepared four types of $A\beta_{1-42}$ assemblies for in vitro experiments: oligomeric Aβ, nitrated oligomeric Aβ, fibrillar Aβ, and nitrated fibrillar Aβ. 1,1,1,3,3,3-hexafluoro-2-propanol (HFIP)-treated $A\beta_{1-42}$ peptide (1 mg; Bachem, cat# 4090148), was dissolved in HFIP and evaporated to form a monomeric film, which was resuspended in DMSO at 5 mM. This solution was further diluted in Dulbecco's modified Eagle's medium (DMEM)/F-12 without phenol red (Gibco, cat# 21041025) to the desired working concentration [39]. Aliquots were then divided for aggregation protocols: oligomerization was induced by incubation under gentle shaking for 48 h at 4°C, whereas fibrillization was induced by incubation under gentle shaking for 6 days at 37°C. Nitration of pre-formed oligomers and fibrils was performed by photoirradiation as previously described [26] with a minor modification of an additional 6h incubation at 37°C under gentle shaking. In short, photoirradiation was performed by placing the assemblies under a red LED light for 30 minutes in the presence of the previously described peroxynitrite-releasing molecule BPT-NO [40]. All experiments were conducted with freshly prepared assemblies, and while different peptide batches were used, the same batch was always maintained within each experimental set.

## ESI-MS analysis of the Aβ-NO adducts

The Aβ-containing assemblies were treated as previously reported [26]. Briefly, assemblies were treated with HFIP and sonicated for 60 min at 37°C for. After centrifugation (5 min at 12,000 g), HFIP was evaporated under nitrogen. Assemblies were resuspended in phosphate buffer (50 mM pH 7.4) and incubated with trypsin (enzyme/protein 1:20 w:w) at 16 h 37°C. The peptide content was analyzed by Liquid Chromatography – Mass Spectrometry (LC – MS), using a Vanquish Ultra High-Performance Liquid Chromatography (UHPLC) system (Thermo Fisher Scientific) equipped with a Hypesil Gold C18 column (2.1 mm × 50 mm, 1.9 µm, Thermo Fisher Scientific). The mobile phase consisted of water (eluent A) and acetonitrile (eluent B), both containing formic acid (0.1%).

The autosampler was maintained at 4°C, and the injection volume was 5 µL. Mass spectrometric detection was performed using a TSQ Quantis (Thermo Fisher Scientific) equipped with an electrospray ion (ESI) source working in positive mode. Mass analysis was performed via single ion monitoring (SIM) of the selected peptide species. Specific parameters were used for sheath gas (30 AU), auxiliar gas (10 AU), ion transfer tube temperature (325°C) and vaporizer temperature (350°C). The extracted ion chromatogram (XIC) due to each charged species of the hydrolytic peptide fragment was used for peak detection. Chromatograms were analyzed using Chromeleon software.

## Dot blot analysis

After the photoirradiation, the presence of nitration on preformed $A\beta_{1-42}$ oligomers and fibrils was confirmed by dot blot analysis. A volume of 1µL of 100µM stock of each assembly was spotted onto a nitrocellulose membrane (0.2 mm, Hybond ECL, Amersham Italia). The same assemblies were also spotted at 1:3 and 1:10 dilutions in DMEM/F-12 without phenol red. Membranes were blocked in Odyssey blocking buffer (LiCor, Biosciences) for 1 hour, then incubated with either anti-Aβ N-terminal 1–16 mouse monoclonal antibody 6E10 (1:100) or rabbit polyclonal anti-nitrotyrosine antibody A-21285 (1:400, BioLegend) overnight at 4°C. Finally, the membrane was repeatedly washed and exposed to the secondary goat anti-mouse or anti-rabbit antibody labeled with IR dye (1:20,000) for 45 min. Hybridization signals were detected with the Odyssey CLx Infrared Imaging System (LI-COR Biosciences, Lincoln, NE). The rabbit polyclonal anti-nitrotyrosine antibody (A-21285) was selected for the dot blot assay because it is compatible with infrared-based membrane detection, whereas the mouse monoclonal antibody HM.11 was used for multiplex immunofluorescence. Both antibodies recognize nitrotyrosine residues rather than Aβ itself; therefore, immunofluorescence analyses were restricted to 3-NT signals co-localizing with Aβ-positive deposits, while dot blot analyses were performed on purified synthetic Aβ preparations.

# Thioflavin-T Assay

We carried out the thioflavin-T assay as previously reported to monitor the effect of nitration on the amyloid-type aggregation of Aβ [41]. Briefly, the $A\beta_{1-42}$ pre-formed oligomers and fibrils, nitrated or not, were incubated with 10 µM of synthetic monomeric $A\beta_{1-42}$ and Thioflavin-T (90µM) in 3% DMSO DMEM/F-12 medium (without phenol red) for 3 days at 37°C. Fluorometric measurements were carried out in triplicate with excitation and emission wavelengths at 450 and 480 nm, respectively, using the multiplate reader Victor Nivo (Milan, Italy).

# Cell cultures and viability assays

Immortalized murine microglial BV2 cells (C57BL/6) were maintained at 37°C in 5% $CO_2$, DMEM, supplemented with 100 µg/mL penicillin/streptomycin antibiotic and 10% fetal bovine serum (FBS). One day before experiments, $1\times10^3$ cells/well (passage ≤18) were seeded in 96-well plates with fresh DMEM containing 10% FBS. All treatments were done in serum-free DMEM, with Aβ assemblies added where indicated at the final concentration of 2 µM. After 72 hours, cell viability was assessed using the MTT assay: cultures were incubated with 0.5 mg/mL 3-(4,5-dimethylthiazol-2-yl)-2,5-diphenyltetrazolium bromide (MTT) solution for 2 hours at 37°C, lysed in DMSO, and the formazan production was evaluated by the Multimode Microplate Reader “Victor Nivo” (Revvity Inc), through the absorbance at 570 nm. Microglial morphology was assessed with an Incucyte®SX1 system (Sartorius), capturing four images per well every 24 hours for 3 days. Morphological phenotypes of amoeboid and rod-shaped were quantified cell-by-cell in Fiji ImageJ2 (version 2.14.0). The model was validated by immunocytochemical staining for CD68 to confirm phagocytosis signals in amoeboid cells (**eFigure 1 in Additional file 1**).

The neuroblastoma cell line, SH-SY5Y, was maintained in DMEM-F12 (GibcoTM, ThermoFisher) supplemented with 10% heat-inactivated (HI) fetal calf serum (GibcoTM, ThermoFisher), 100 mg/mL penicillin and streptomycin (Gibco, ThermoFisher), and 2 mM L-glutamine at 37°C, 5% $CO_2$. Two weeks before experiments, $5\times10^3$ cells were plated on 96-well plates in DMEM-F12 with 5% HI fetal calf serum. The percentage of serum was gradually decreased until it was 1% of the total. All-trans-retinoic acid (RA), 5 µM, was used to promote neuronal differentiation, and the medium containing RA was changed every three days. Fully differentiated SH-

SY5Y cells were treated with Aβ assemblies at the final concentration of 2 µM where needed. After 48h treatment, cell cultures were incubated with 0.5 mg/mL MTT for 2 hours at 37°C, lysed in DMSO, and the formazan production was evaluated by the Multimode Microplate Reader “Victor Nivo” (Revvity Inc), through the absorbance at 570 nm.

# Statistical analysis

For tissue analyses, the outcome variable was the pixel percentage of each immunofluorescent-stained marker, converted to a proportion (0–1) prior to analysis. Descriptive statistics for these measurements are reported as medians [interquartile ranges (IQR)]. Group-level effects on marker burden were evaluated using linear mixed-effects models with deposit group as fixed effect and case as random intercept to account for multiple annotations within subjects:

$$Marker\ proportion_{\{ij\}} \sim\ Group_{\{i\}} + \ \left(1\ \mid Case_{\{j\}}\right)$$

Models were estimated using the lmer function in the lme4 package. Fixed effects were tested with Type III ANOVA using Satterthwaite’s approximation for denominator degrees of freedom (lmerTest package). When ANOVA indicated a significant group effect, we ran pairwise comparisons using estimated marginal means (emmeans package), corrected for multiple comparisons using the false discovery rate (FDR; Benjamini–Hochberg procedure). Model assumptions including normality of residuals, homoscedasticity, and influence of individual data points were evaluated using Q–Q plots, residual plots, and fitted vs. residual plots. Diagnostic plots for model fit indicated approximately constant variance and mild tail deviations from normality in the residuals. As linear mixed models are robust to moderate departures from normality, we retained this model for inference. Tissue analyses were performed in R version 4.5.1 (R Core Team, Vienna, Austria) using RStudio (2025.05.1).

For in vitro experiments (2–4 replicates per condition) statistical significance was tested using one-way ANOVA, and Tukey’s post-hoc test, performed in GraphPad Prism, version 10. A p-value < 0.05 was considered statistically significant.

## Results

# Aβ species distribution across deposit types

We analyzed several Aβ species targeting distinct regions or PTMs along the $Aβ_{1-42}$ sequence (Fig. 1): $Aβ_{aa1-x}$, $Aβ_{N3pE}$, pSer8-Aβ, and 3-NT. Their distribution across deposit types is shown in Fig. 2, and detailed statistical outcomes for each pairwise comparison are provided in **Additional file 2**.

**$Aβ_{aa1-x}$**. Diffuse plaques had the lowest $Aβ_{aa1-x}$ immunoreactivity among all deposit types (Fig. 2). In contrast, classic cored plaques and coarse-grained plaques both showed strong $Aβ_{aa1-x}$ labeling, with median pixel positivity exceeding 30% of the analyzed area. In classic cored plaques, the highest burden was in the plaques’ core (Fig. 3). The highest $Aβ_{aa1-x}$ values were observed in CAA, particularly in capCAA (88% [82%-93%]), indicating prominent accumulation of Aβ within vessel walls.

**Aβ $_{N3pE}$** . $Aβ_{N3pE}$ was detectable in diffuse plaques, but its reactivity did not differ significantly from that in control tissue (Fig. 2; **Additional file 2**). Classic cored and coarse-grained plaques showed higher $Aβ_{N3pE}$ values than controls but remained lower than that in CAA. Within classic cored plaques, $Aβ_{N3pE}$ localized predominantly to the dense core rather than the corona (Fig. 3). Among CAA subtypes, capCAA showed the greatest burden (91% [81%-97%]), followed by larger-vessel CAA (72% [62%-80%]). Leptomeningeal CAA displayed intermediate values (43% [29%-58%]), comparable to those of classic cored and coarse-grained plaques.

**pSer8-Aβ**. pSer8-Aβ was present in diffuse plaques, though at lower levels than AβN3pE; however, its total reactivity did not differ significantly from that in control tissue. Similar to $Aβ_{N3pE}$, pSer8-Aβ immunoreactivity was higher in classic cored and coarse-grained plaques, with signal concentrated within the plaque core (Fig. 3). CapCAA and larger-vessel CAA again had the highest values (72% [52%-80%] and 63% [53%-73%], respectively), whereas leptomeningeal CAA (27% [16%-47%]) showed levels comparable to those seen in classic cored plaques.

**3-NT**. 3-NT immunoreactivity, measured using two triple-stain combinations ($Aβ_{aa1-x}$ + $Aβ_{N3pE}$ + 3-NT and $Aβ_{aa1-x}$ + pSer8-Aβ + 3-NT), showed a consistent pattern across assays. Diffuse plaques showed negligible 3-NT signal, and although detectable staining was present in classic cored and coarse-grained plaques, values were not significantly different from those in control tissue (Fig. 2; **Additional file 2**). In contrast, all CAA categories demonstrated elevated 3-NT levels compared to both control tissue and parenchymal plaques, with larger-vessel (49% [36%-61%]) and leptomeningeal CAA (50% [34%-64%]) displaying the highest burden. Vessels without CAA did not show any relevant positivity to 3-NT (**eFigure 2 in Additional file 1**). Among the examined PTMs, 3-NT showed a compartment-specific pattern, being markedly enriched in the vasculature—especially in leptomeningeal and larger-vessel CAA—whereas AβN3pE and pSer8-Aβ were broadly distributed across parenchymal plaques and CAA, peaking in capCAA.

**3-NT-Aβ associates with the presence of β-pleated sheets in Aβ deposits**

Thioflavin-S staining confirmed the deposit classification, depicting amyloid in a β-pleated sheet conformation in classic cored plaques, coarse-grained plaques, and CAA, but not in diffuse plaques (Fig. 4a). Using the triple combination $Aβ_{aa1-x}$/3-NT/thioflavin-S, we found that 3-NT immunoreactivity was negligible in diffuse plaques, whereas 3-NT and thioflavin-S signals showed near-complete overlap across all fibrillar Aβ deposits (Fig. 4a, b), with the highest 3-NT signal observed in CAA. In classic cored plaques, differential analysis of the core and corona confirmed that the fibrillar structure and 3-NT were mostly restricted to the core (Fig. 3).

To enable comparison of Aβ species immunolabeling and fibril content across deposits, a qualitative heatmap summarizing staining intensity is presented in Fig. 5. In this heatmap, each row corresponds to a distinct Aβ deposit, and each column represents a different Aβ species, 3-NT or thioflavin-S.

Following these findings, we performed in vitro thioflavin-T (ThT) assays to investigate the influence of nitration on both oligomeric and fibril Aβ aggregation. As shown in Fig. 4c, ThT assays indicated that nitration delayed the aggregation of oligomeric Aβ species, but accelerated fibrillation of preformed fibrils relative to non-nitrated controls. Nitration was achieved using the BPT-NO irradiation method described previously [23], which generates peroxynitrite and induces a defined level of tyrosine nitration (~ 0.45‰) sufficient to redirect Aβ

monomer aggregation away from fibrillation. Using this same approach, dot blot analysis with an anti-nitrotyrosine antibody confirmed that BPT-NO irradiation nitrated both oligomeric and fibrillar Aβ species (Fig. 4d; **full blot in Additional file 3**). UHPLC-MS analysis of trypsin-digested assemblies specifically detected the nitrated peptide fragment $Aβ_{6-16}$–$NO_2$ only in irradiated $Aβ_{1-42}$/BPT-NO mixtures. To provide an estimate of the nitration level, we calculated the ratio of the chromatographic peak area of $Aβ_{6-16}$–$NO_2$ to that of its unmodified counterpart, $Aβ_{6-16}$. The extent of nitration was similar in both oligomeric and fibrillar forms of Aβ (**eTable 2 in Additional file 1**), suggesting that tyrosine in position 10 exhibits comparable accessibility to nitration in both in vitro aggregation states.

# Nitration of Aβ fibrils sustains microglia activation

Because microglial activation is a key feature of Aβ pathology and nitration may modulate this response, we quantified CD68 immunoreactivity in distinct deposits. The neuroinflammatory CD68 profile resembled the 3-NT distribution. Diffuse plaques showed negligible CD68, comparable to control levels, indicating limited microglial engagement in these aggregates (Fig. 6a-b; **Additional file 2**). In contrast, classic cored plaques showed the highest immunoreactivity among all deposits, with CD68 located in between the core and the corona. Coarse-grained plaques showed slightly less immunoreactivity, with the microglia appearing as smaller dots dispersed throughout the plaque. In CAA, CD68 positivity was more variable than in parenchymal plaques, with the lowest CD68 immunoreactivity observed in capCAA and the highest in larger-vessel CAA.

Given the co-occurrence of fibrillar plaques (coarse-grained and classic cored plaques), 3-NT, and activated microglia in tissue, we investigated how nitration affects Aβ-induced microglial activation in vitro. All four Aβ conditions—nitrated and non-nitrated oligomers and fibrils—triggered the differentiation of BV2 cells into an amoeboid, phagocytic-like phenotype (Fig. 6c). By 72 hours post-treatment, cells in all conditions had largely shifted toward a rod-shaped morphology; however, the amoeboid morphology persisted significantly longer only in cells treated with nitrated fibrils. No reduction in BV2 cell viability was detected, consistent with a dynamic cellular response rather than toxicity (**eFigure 3 in Additional file 1**). These in vitro results align with our histological data showing both nitration and CD68 immunoreactivity in plaque types containing a fibrillar component, further suggesting that nitrated Aβ fibrils induce a more sustained microglial activation than their non-nitrated counterparts.

# Nitration of Aβ does not increase toxicity in SH-SY5Y neurons

Finally, to test whether nitration could influence the toxicity of Aβ on neuronal cells, we conducted viability assays using the human neuroblastoma cell line SH-SY5Y, differentiated into a neuron-like state. After 48h treatment, Aβ fibrils were neurotoxic to the same extent as Aβ oligomers (**eFigure 4 in Additional file 1**). Nitrated Aβ oligomers and nitrated Aβ fibrils showed similar toxic effects as their non-nitrated counterparts. (**eFigure 4 in Additional file 1**).

## Discussion

In this study, we characterized PTMs in parenchymal and vascular Aβ deposits in AD and considering our neuropathologic survey, examined the functional impact of nitration. Our main finding is that PTMs are not uniformly distributed but, instead, follow compartment-specific patterns: phosphorylation (pSer8-Aβ) and pyroglutamylation ($Aβ_{N3pE}$) broadly label fibrillar parenchymal plaques and vascular amyloid, whereas nitration

(3-NT) is enriched in vascular deposits, particularly larger-vessel and leptomeningeal CAA. To gain insight into the functional significance of nitration, we performed in vitro experiments in which preformed Aβ assemblies were nitrated and then tested for their effects on aggregation, microglial activation, and neuronal viability. These experiments revealed that nitration slowed oligomer-to-fibril conversion but accelerated the growth of pre-existing fibrils, sustained microglial activation without inducing direct neurotoxicity.

Our tissue analysis supports a molecular continuum from early to mature deposits in the parenchyma. Diffuse plaques showed trace amounts of $Aβ_{N3pE}$ and pSer8-Aβ and negligible 3-NT, consistent with their proposed role as early-stage, relatively unmodified assemblies. Classic cored and coarse-grained plaques showed comparable enrichment of $Aβ_{N3pE}$ and pSer8-Aβ, indicating that these N-terminal PTMs mark fibrillar parenchymal deposits in general rather than distinguishing between plaque subtypes [14, 17, 42, 43]. However, whereas $Aβ_{N3pE}$ and pSer8-Aβ were confined to the dense core in classic cored plaques, they were distributed throughout the deposit in coarse-grained [11]. Phosphorylation at serine-8 has been shown to stabilize β-sheet structure and promote fibril formation [44], consistent with its enrichment in fibrillar plaque types [11]. Fibrillar plaques showed low but detectable 3-NT within their cores, suggesting that nitration arises in vivo once fibrillar organization is established [25]. While a recent neuropathologic study reported intraneuronal 3-NT signal but minimal plaque immunoreactivity using a monoclonal clone (4C3) on 40 µm free-floating sections[17], our detection of 3-NT co-localized with $Aβ_{aa1-x}$ in fibrillar plaque cores is consistent with previous observations [25]. Methodological variations, including section thickness (40 vs 5 µm thick tissue), antigen retrieval protocols, and antibody clone selectivity, likely influence the unmasking of sterically buried N-terminal epitopes within dense cross β-sheet cores. Furthermore, transmission electron microscopy immunogold analysis in that same study[17] confirmed that 3-NT-Aβ assemblies integrate into fibrillar amyloid, providing structural support for its presence within extracellular plaque cores. Together these tissue-level findings extend recent proteomic data on $Aβ_{40}$ and pyroglutamated species[14] and complement work on spontaneous molecular aging modifications such as L-isoaspartate formation (isoAsp7-Aβ)[15, 45] by incorporating phosphorylation and nitration into the maturation trajectory of parenchymal deposits.

While a sequential biochemical maturation (e.g., Aβ → $Aβ_{N3pE}$ → pSer8-Aβ) has been proposed for parenchymal tissue deposits [43] our data show that vascular deposits exhibit a distinct, vessel-bed–specific modification profile characterized by higher nitration. CapCAA exhibited the highest relative levels of $Aβ_{N3pE}$ and pSer8-Aβ with minimal 3-NT, pointing to predominant enzymatic PTMs. In contrast, larger-vessel and leptomeningeal CAA retained robust $Aβ_{N3pE}$ and pSer8-Aβ yet showed higher 3-NT than capCAA. This pattern plausibly reflects slower perivascular clearance, reduced astrocytic ensheathment [46, 47], and greater exposure to perivascular macrophage-derived nitric oxide/peroxynitrite [48, 49] in these larger vessels. Thus, local clearance and the oxidative milieu appear to determine whether vascular Aβ is primarily enzymatically modified or additionally subjected to nitration.

Our histological and in vitro data provide a kinetic explanation for this compartment-specific 3-NT enrichment. Thioflavin-S staining showed near-complete overlap between 3-NT and fibrillar amyloid, and our in vitro thioflavin-T assays revealed that nitration slowed the conversion of Aβ oligomers into fibrils yet accelerated the growth of pre-formed fibrils. Together, these data suggest that nitration does not initiate aggregation but rather stabilizes and promotes the expansion of existing fibrillar assemblies. The strong enrichment of 3-NT in

vascular amyloid, where fibrillar organization is highly ordered, further supports that nitration reflects late-stage deposit maturation and compartmental specialization.

The relationship between nitration and neuroinflammation was then examined. The distribution of CD68-positive microglia in tissue resembled that of 3-NT, being negligible in diffuse plaques and prominent in fibrillar plaque types and larger-vessel and leptomeningeal CAA. In vitro, all Aβ assemblies transiently induced an amoeboid microglial phenotype, but this response was prolonged only by nitrated fibrils. These findings support a feed-forward model in which fibrillar Aβ activates microglia [50], promoting the release of nitric oxide and peroxynitrite that, in turn, nitrate Aβ and sustain microglial engagement. Within this cycle, nitration appears to maintain a localized state of chronic inflammatory activation rather than initiating it. Importantly, while prior work has implicated TREM2 in recognizing phosphorylated Aβ [51], the prolonged response to nitrated fibrils in our BV2 cells likely involves TREM2-independent pathways, as nitrated Aβ has not been shown to enhance TREM2 binding [51]. Finally, we tested whether nitration influences direct neuronal toxicity. Using neuronally differentiated SH-SY5Y cells, we found that nitrated Aβ oligomers and fibrils showed similar toxic effects as their non-nitrated counterparts. Hence, nitration of Aβ fibrils exerts cell-type-specific effects: it prolongs microglial activation without directly increasing neuronal toxicity.

Several limitations should be acknowledged. A key technical consideration concerns the interpretation of 3-NT immunoreactivity. The anti-nitrotyrosine antibody used is not specific for nitrated Aβ, as it recognizes nitrotyrosine residues on any protein. To ensure that our tissue-based 3-NT signal specifically reflected nitrated Aβ rather than general nitrative stress, we employed a stringent masking approach. We analyzed 3-NT immunoreactivity exclusively within the context of triple co-staining, and only 3-NT signals that colocalized with Aβ ($Aβ_{aa1-x}$) were quantified. This approach allows us to confidently attribute the observed 3-NT enrichment in CAA and fibrillar plaques to the amyloid milieu. The in vitro nitration model based on BPT-NO photoirradiation, while controlled, may not fully replicate the complex oxidative environment in vivo. Furthermore, BV2 microglia and SH-SY5Y neuronal-like cells, though standard first-line screening models, do not fully capture the complexity of the human brain microenvironment. While multiplex immunofluorescence does not provide absolute biochemical quantification of individual Aβ species, it preserves their spatial context, enabling direct comparison of PTM distribution across distinct plaque morphologies and vascular compartments. This spatial information is essential for identifying PTM patterns across distinct Aβ deposits, such as the preferential enrichment of 3-NT within vascular amyloid observed in the present study. Like all analyses performed on thin histological sections, immunofluorescence detects antigens exposed at the cut surface and therefore does not provide a volumetric assessment of entire plaques. Because plaques are intersected at random positions during sectioning, however, the quantified plaques represent a range of sectioning depths through their three-dimensional structure. Although each individual measurement reflects only a single sectioning plane, this random sampling reduces systematic bias associated with any particular cutting plane. The consistent spatial enrichment patterns observed across plaques and cases suggest that the relative differences reported here are robust despite this inherent limitation. In contrast, biochemical approaches such as LC-MS/MS or multiplex ELISA provide absolute quantification of PTMs but require tissue homogenization, thereby sacrificing information regarding plaque architecture and regional localization. These approaches should therefore be regarded as complementary rather than competing methodologies. Future studies integrating regional microdissection with mass spectrometric profiling and spatial digital pathology will provide both absolute PTM quantification and high-resolution anatomical context across the spectrum of AD pathology.

Nonetheless, the convergence of our tissue mapping data with mechanistic in vitro assays strengthens the conclusion that nitration is a compartment-specific modification linked to vascular amyloid and sustained microglial activation. This compartmentalization of 3-NT to vascular Aβ deposits, particularly leptomeningeal and larger-vessel CAA, suggests a potential diagnostic application. A fluid assay targeting 3-NT–Aβ could index vascular nitro-oxidative stress and serve as a biomarker for CAA burden, a pathology that is difficult to assess with current amyloid PET or standard plasma Aβ assays yet strongly predicts ARIA in the context of anti-Aβ immunotherapy. Sensitive quantification of nitrated peptides in CSF and plasma has already been demonstrated [52, 53]. By capturing a compartment-specific oxidative signature rather than total Aβ load, 3-NT–Aβ could provide a biochemical window into CAA pathology in the era of disease-modifying therapy. Moreover, because 3-NT–Aβ is differentially enriched across CAA subtypes, such an assay might also help discriminate between capCAA and leptomeningeal CAA, potentially offering insights into differential ARIA risk or pathogenic mechanisms, though this remains speculative and requires prospective validation.

## Conclusions

Together, these findings show that PTMs across Aβ deposits exhibit compartment-specific patterns reflecting distinct biochemical environments. Phosphorylation and pyroglutamylation label parenchymal fibrillar maturation, whereas nitration defines vascular amyloid and sustained microglial activation. By integrating neuropathology with mechanistic assays, our study reveals that Aβ modifications follow compartment- and assembly-specific pathways likely linked to inflammation, underscoring that Aβ heterogeneity in AD reflects local tissue context rather than uniform progression. Replicating these findings across clinical stages and brain regions will help pinpoint when these changes emerge. Finally, 3-NT emerges as an Aβ modification that may help distinguish CAA, providing a rationale for future biomarker studies, particularly in the context of anti-Aβ immunotherapy and ARIA.

## Abbreviations

3-NT 3’-nitrotyrosine

Aβ amyloid-beta

AβN3pE pyroglutamate Aβ at the 3$^{rd}$ amino acid

AD Alzheimer’s disease

ARIA amyloid-related imaging abnormalities

BSA bovine serum albumin

BPT-NO benzophenothiazine-nitric oxide hybrid

CAA cerebral amyloid angiopathy

capCAA capillary cerebral amyloid angiopathy

DMEM Dulbecco’s Modified Eagle’s Medium

DMSO dimethyl sulfoxide

ESI electrospray ion

FBS fetal bovine serum

FDR false discovery rate

FF fresh-frozen

FFPE formalin-fixed (4%) paraffin-embedded

HI heat-inactivated

HFIP 1,1,1,3,3,3-hexafluoro-2-propanol

IQR interquartile ranges

LC-MS liquid chromatography – mass spectrometry

MTT 3-(4,5-dimethylthiazol-2-yl)-2,5-diphenyltetrazolium bromide

NIA-AA National Institute on Aging-Alzheimer's Association

NBB Netherlands brain bank

pSer8-Aβ phosphorylated Aβ at serine 8

PTM post-translational modification

RA all-trans-retinoic acid

SIM single ion monitoring

TBS tris-buffered saline

ThT Thioflavin-T

UHPLC ultra high-performance liquid chromatography

XIC extracted ion chromatogram

## Declarations

# Competing Interests

FS, SZ, SMMV, FB, CP, SS, JW, MLG, AJMR declare they have no competing interests. SB has received travel support to attend scientific meetings. JJMH is employed by F. Hoffmann-La Roche. AC reports no conflicts of

interest. BDCB receives research support from Alzheimer Nederland, the BrightFocus Foundation, and the Mayo Clinic Alzheimer's Disease Research Center. She has received honoraria from F. Hoffmann-La Roche and travel support to attend scientific meetings.

## Consent statement

In compliance with all ethical standards, brain donors or their next of kin signed informed consent regarding the usage of their brain tissue and clinical records for research purposes. The brain donor program is approved by the medical ethics committee of the Amsterdam UMC and conducted in accordance with the Declaration of Helsinki.

## Funding

Research reported in this publication was supported by Alzheimer Nederland WE.06-2023-01 (Principal Investigator [PI]: BDCB), WE.03-2021-15 (PI:BDCB), a Developmental Project subaward from the Mayo Clinic Alzheimer's Disease Research Center (NIA P30 AG062677, PI subaward: BDCB), the BrightFocus Foundation (A2025020S, PI: BDCB), and the Deutsche Forschungsgemeinschaf (WA1477/6–6, PI: JW). Funders had no role in study design, data analysis, or publication decisions.

## Author Contribution

SB, AC, and BDCB accessed and verified the data in the study and take responsibility for the integrity of the data and the accuracy. SB, AC, and BDCB conceived the concept and designed the study. SB and BDCB coordinated the study and were responsible for writing the manuscript. SB, FS, SZ, SMMV, FB, MLG, JJMH, AC, and BDCB were responsible for acquiring, analyzing, or interpretating data. SB, FS, SZ, SMMV, FB, CP, SS, JW, MLG, AJMR, JJMH, AC, and BDCB critically reviewed the manuscript for important intellectual content. SMMV and AJMR were responsible for the autopsy material and neuropathological evaluation. All authors approved the manuscript and take responsibility for the decision to submit for publication.

## Acknowledgement

We would like to acknowledge all brain donors and their caregivers for their generous brain donations to advance our understanding of Alzheimer's disease. We thank the Netherlands Brain Bank (NBB) for providing well-defined brain tissue. The authors thank the PhD Program in Neuroscience, University of Catania, for the doctoral scholarship and for funding S.B.'s research stay abroad. We thank Giuseppe Di Natale, Tjado Morrema and the Microscopy and Cytometry Core Facility at Amsterdam UMC for technical assistance. We gratefully acknowledge Prof. Carsten Korth for providing the IC16 antibody.

## Data Availability

The data supporting the findings of this study are available within the article and its Supplementary Information. Additional data generated and analyzed during the current study, including quantitative immunofluorescence and in vitro experimental data, are available from the corresponding author upon reasonable request.

## References


1. Selkoe DJ, Hardy J. The amyloid hypothesis of Alzheimer's disease at 25 years. EMBO Mol Med. 2016;8:595–608. https://doi.org/10.15252/emmm.201606210.
2. Giuffrida ML, Caraci F, Pignataro B, Cataldo S, De Bona P, Bruno V, et al. β-amyloid monomers are neuroprotective. J Neurosci. 2009;29:10582–7. https://doi.org/10.1523/JNEUROSCI.1736-09.2009.
3. Ono K, Watanabe-Nakayama T. Aggregation and structure of amyloid β-protein. Neurochem Int. 2021;151:105208. https://doi.org/10.1016/j.neuint.2021.105208.
4. Walker JM, Dehkordi SK, Schaffert J, Goette W, White CL III, Richardson TE, et al. The Spectrum of Alzheimer-Type Pathology in Cognitively Normal Individuals. J Alzheimer's Disease. 2023;91:683–95. https://doi.org/10.3233/JAD-220898.
5. Morris GP, Clark IA, Vissel B. Questions concerning the role of amyloid-β in the definition, aetiology and diagnosis of Alzheimer's disease. Acta Neuropathol. 2018;136:663–89. https://doi.org/10.1007/s00401-018-1918-8.
6. Tomassen J, den Braber A, van der Lee SJ, Reus LM, Konijnenberg E, Carter SF, et al. Amyloid-β and APOE genotype predict memory decline in cognitively unimpaired older individuals independently of Alzheimer's disease polygenic risk score. BMC Neurol. 2022;22:484. https://doi.org/10.1186/s12883-022-02925-6.
7. Vidoni ED, Yeh H-W, Morris JK, Newell KL, Alqahtani A, Burns NC, et al. Cerebral β-Amyloid Angiopathy Is Associated with Earlier Dementia Onset in Alzheimer's Disease. Neurodegener Dis. 2016;16:218–24. https://doi.org/10.1159/000441919.
8. Boyle PA, Yu L, Nag S, Leurgans S, Wilson RS, Bennett DA, et al. Cerebral amyloid angiopathy and cognitive outcomes in community-based older persons. Neurology. 2015;85:1930–6. https://doi.org/10.1212/WNL.0000000000002175.
9. Hecht M, Krämer LM, von Arnim CAF, Otto M, Thal DR. Capillary cerebral amyloid angiopathy in Alzheimer's disease: association with allocortical/hippocampal microinfarcts and cognitive decline. Acta Neuropathol. 2018;135:681–94. https://doi.org/10.1007/s00401-018-1834-y.
10. Röhr D, Boon BDC, Schuler M, Kremer K, Hoozemans JJM, Bouwman FH, et al. Label-free vibrational imaging of different Aβ plaque types in Alzheimer's disease reveals sequential events in plaque development. Acta Neuropathol Commun. 2020;8:222. https://doi.org/10.1186/s40478-020-01091-5.
11. Boon BDC, Bulk M, Jonker AJ, Morrema THJ, van den Berg E, Popovic M, et al. The coarse-grained plaque: a divergent Aβ plaque-type in early-onset Alzheimer's disease. Acta Neuropathol Springer Sci Bus Media Deutschland GmbH. 2020;140:811–30. https://doi.org/10.1007/s00401-020-02198-8.
12. Boon BDC, Piura YD, Moloney CM, Chalk JL, Lincoln SJ, Rutledge MH, et al. Neuropathological changes and amyloid-related imaging abnormalities in Alzheimer's disease treated with aducanumab versus untreated: a retrospective case–control study. Lancet Neurol. 2025;24:931–44. https://doi.org/10.1016/S1474-4422(25)00313-8.

13. Lochocki B, Boon BDC, Verheul SR, Zada L, Hoozemans JJM, Ariese F, et al. Multimodal, label-free fluorescence and Raman imaging of amyloid deposits in snap-frozen Alzheimer's disease human brain tissue. Commun Biol Nat Res. 2021;4. https://doi.org/10.1038/s42003-021-01981-x.
14. Koutarapu S, Ge J, Dulewicz M, Srikrishna M, Szadziewska A, Wood J, et al. Chemical imaging delineates Aβ plaque polymorphism across the Alzheimer's disease spectrum. Nat Commun. 2025;16:3889. https://doi.org/10.1038/s41467-025-59085-7.
15. Gnoth K, Piechotta A, Kleinschmidt M, Konrath S, Schenk M, Taudte N, et al. Targeting isoaspartate-modified Aβ rescues behavioral deficits in transgenic mice with Alzheimer's disease-like pathology. Alzheimers Res Ther. 2020;12:149. https://doi.org/10.1186/s13195-020-00719-x.
16. Schaffert L-N, Carter WG. Do Post-Translational Modifications Influence Protein Aggregation in Neurodegenerative Diseases: A Systematic Review. Brain Sci. 2020;10:232. https://doi.org/10.3390/brainsci10040232.
17. Schrempel S, Kottwitz AK, Piechotta A, Gnoth K, Büschgens L, Hartlage-Rübsamen M, et al. Identification of isoAsp7-Aβ as a major Aβ variant in Alzheimer's disease, dementia with Lewy bodies and vascular dementia. Acta Neuropathol. 2024;148:78. https://doi.org/10.1007/s00401-024-02824-9.
18. Querfurth HW, LaFerla FM. Alzheimer's disease. N Engl J Med. 2010;362:329–44. https://doi.org/10.1056/NEJMra0909142.
19. Heneka MT, Carson MJ, Khoury J, El, Landreth GE, Brosseron F, Feinstein DL, et al. Neuroinflammation in Alzheimer's disease. Lancet Neurol. 2015;14:388–405. https://doi.org/10.1016/S1474-4422(15)70016-5.
20. Leng F, Edison P. Neuroinflammation and microglial activation in Alzheimer disease: where do we go from here? Nat Rev Neurol. 2021;17:157–72. https://doi.org/10.1038/s41582-020-00435-y.
21. Glass CK, Saijo K, Winner B, Marchetto MC, Gage FH. Mechanisms underlying inflammation in neurodegeneration. Cell. 2010;140:918–34. https://doi.org/10.1016/j.cell.2010.02.016.
22. Hampel H, Caraci F, Cuello AC, Caruso G, Nisticò R, Corbo M, et al. A Path Toward Precision Medicine for Neuroinflammatory Mechanisms in Alzheimer's Disease. Front Immunol. 2020;11:456. https://doi.org/10.3389/fimmu.2020.00456.
23. Heppner FL, Ransohoff RM, Becher B. Immune attack: the role of inflammation in Alzheimer disease. Nat Rev Neurosci. 2015;16:358–72. https://doi.org/10.1038/nrn3880.
24. Radi R. Nitric oxide, oxidants, and protein tyrosine nitration. Proc Natl Acad Sci U S A. 2004;101:4003–8. https://doi.org/10.1073/pnas.0307446101.
25. Kummer MP, Hermes M, Delekarte A, Hammerschmidt T, Kumar S, Terwel D, et al. Nitration of tyrosine 10 critically enhances amyloid β aggregation and plaque formation. Neuron. 2011;71:833–44. https://doi.org/10.1016/j.neuron.2011.07.001.
26. Basile S, Parisi C, Bellia F, Zimbone S, Arrabito G, Gulli D, et al. Red-Light-Photosensitized Tyrosine 10 Nitration of β-Amyloid1-42 Diverts the Protein from Forming Toxic Aggregates. ACS Chem Neurosci. 2024;15:2916–24. https://doi.org/10.1021/acschemneuro.4c00284.
27. Montine TJ, Phelps CH, Beach TG, Bigio EH, Cairns NJ, Dickson DW, et al. National Institute on Aging–Alzheimer's Association guidelines for the neuropathologic assessment of Alzheimer's disease: a practical approach. Acta Neuropathol. 2012;123:1–11. https://doi.org/10.1007/s00401-011-0910-3.

28. Braak H, Braak E. Neuropathological stageing of Alzheimer-related changes. Acta Neuropathol. 1991;82:239–59. https://doi.org/10.1007/BF00308809.
29. Thal DR, Rüb U, Schultz C, Sassin I, Ghebremedhin E, Del Tredici K, et al. Sequence of Aβ-Protein Deposition in the Human Medial Temporal Lobe. J Neuropathol Exp Neurol. 2000;59:733–48. https://doi.org/10.1093/jnen/59.8.733.
30. DeTure MA, Dickson DW. The neuropathological diagnosis of Alzheimer's disease. Mol Neurodegener. 2019;14:32. https://doi.org/10.1186/s13024-019-0333-5.
31. Boon BDC, Hoozemans JJM, Lopuhaä B, Eigenhuis KN, Scheltens P, Kamphorst W, et al. Neuroinflammation is increased in the parietal cortex of atypical Alzheimer's disease. J Neuroinflammation BioMed Cent Ltd. 2018;15. https://doi.org/10.1186/s12974-018-1180-y.
32. Bourassa P, Tremblay C, Schneider JA, Bennett DA, Calon F. Beta-amyloid pathology in human brain microvessel extracts from the parietal cortex: relation with cerebral amyloid angiopathy and Alzheimer's disease. Acta Neuropathol. 2019;137:801–23. https://doi.org/10.1007/s00401-019-01967-4.
33. Müller-Schiffmann A, März-Berberich J, Andreyeva A, Rönicke R, Bartnik D, Brener O, et al. Combining Independent Drug Classes into Superior, Synergistically Acting Hybrid Molecules. Angew Chem Int Ed. 2010;49:8743–6. https://doi.org/10.1002/anie.201004437.
34. Kumar S, Walter J. Phosphorylation of amyloid beta (Aβ) peptides – A trigger for formation of toxic aggregates in Alzheimer's disease. Aging. 2011;3:803–12. https://doi.org/10.18632/aging.100362.
35. Dornieden S, Müller-Schiffmann A, Sticht H, Jiang N, Cinar Y, Wördehoff M, et al. Characterization of a Single-Chain Variable Fragment Recognizing a Linear Epitope of Aβ: A Biotechnical Tool for Studies on Alzheimer's Disease? PLoS ONE. 2013;8:e59820. https://doi.org/10.1371/journal.pone.0059820.
36. Müller-Schiffmann A, März-Berberich J, Andreyeva A, Rönicke R, Bartnik D, Brener O, et al. Combining independent drug classes into superior, synergistically acting hybrid molecules. Angew Chem Int Ed Engl. 2010;49:8743–6. https://doi.org/10.1002/anie.201004437.
37. Talucci I, Leske T, Klafki H-W, Hassan MM, Steiert A, Morgado B, et al. Aggregation-dependent epitope sequence and modification fingerprints of anti-Aβ antibodies. Elife. 2026;14. https://doi.org/10.7554/eLife.106156.3.
38. Kumar S, Wirths O, Theil S, Gerth J, Bayer TA, Walter J. Early intraneuronal accumulation and increased aggregation of phosphorylated Abeta in a mouse model of Alzheimer's disease. Acta Neuropathol. 2013;125:699–709. https://doi.org/10.1007/s00401-013-1107-8.
39. Lambert MP, Barlow AK, Chromy BA, Edwards C, Freed R, Liosatos M et al. Diffusible, nonfibrillar ligands derived from A 1–42 are potent central nervous system neurotoxins [Internet]. 1998.
40. Parisi C, Failla M, Fraix A, Menilli L, Moret F, Reddi E, et al. A generator of peroxynitrite activatable with red light. Chem Sci. 2021;12:4740–6. https://doi.org/10.1039/d0sc06970a.
41. Greco V, Naletova I, Ahmed IMM, Vaccaro S, Messina L, La Mendola D, et al. Hyaluronan-carnosine conjugates inhibit Aβ aggregation and toxicity. Sci Rep. 2020;10:15998. https://doi.org/10.1038/s41598-020-72989-2.
42. Li X, Ospitalieri S, Robberechts T, Hofmann L, Schmid C, Rijal Upadhaya A, et al. Seeding, maturation and propagation of amyloid β-peptide aggregates in Alzheimer's disease. Brain. 2022;145:3558–70. https://doi.org/10.1093/brain/awac202.

43. Gerth J, Kumar S, Rijal Upadhaya A, Ghebremedhin E, von Arnim CAF, Thal DR, et al. Modified amyloid variants in pathological subgroups of β-amyloidosis. Ann Clin Transl Neurol. 2018;5:815–31. https://doi.org/10.1002/acn3.577.
44. Kumar S, Rezaei-Ghaleh N, Terwel D, Thal DR, Richard M, Hoch M, et al. Extracellular phosphorylation of the amyloid β-peptide promotes formation of toxic aggregates during the pathogenesis of Alzheimer's disease. EMBO J. 2011;30:2255–65. https://doi.org/10.1038/emboj.2011.138.
45. Mukherjee S, Coyle R, Dubois C, Perez K, McLean C, Masters CL, et al. Isomerized Aβ in the brain can distinguish the status of amyloidosis in the Alzheimer's disease spectrum. Acta Neuropathol. 2025;150:7. https://doi.org/10.1007/s00401-025-02914-2.
46. Kaur J, Fahmy LM, Davoodi-Bojd E, Zhang L, Ding G, Hu J, et al. Waste Clearance in the Brain. Front Neuroanat. 2021;15. https://doi.org/10.3389/fnana.2021.665803.
47. Moretti R, Caruso P. Small Vessel Disease-Related Dementia: An Invalid Neurovascular Coupling? Int J Mol Sci. 2020;21:1095. https://doi.org/10.3390/ijms21031095.
48. Wen W, Cheng J, Tang Y. Brain perivascular macrophages: current understanding and future prospects. Brain. 2024;147:39–55. https://doi.org/10.1093/brain/awad304.
49. Manu DR, Slevin M, Barcutean L, Forro T, Boghitoiu T, Balasa R. Astrocyte Involvement in Blood–Brain Barrier Function: A Critical Update Highlighting Novel, Complex, Neurovascular Interactions. Int J Mol Sci. 2023;24:17146. https://doi.org/10.3390/ijms242417146.
50. Sebastian Monasor L, Müller SA, Colombo AV, Tanrioever G, König J, Roth S, et al. Fibrillar Aβ triggers microglial proteome alterations and dysfunction in Alzheimer mouse models. Elife. 2020;9. https://doi.org/10.7554/eLife.54083.
51. Joshi P, Riffel F, Satoh K, Enomoto M, Qamar S, Scheiblich H, et al. Differential interaction with TREM2 modulates microglial uptake of modified Aβ species. Glia. 2021;69:2917–32. https://doi.org/10.1002/glia.24077.
52. Tohgi H, Abe T, Yamazaki K, Murata T, Ishizaki E, Isobe C. Alterations of 3-nitrotyrosine concentration in the cerebrospinal fluid during aging and in patients with Alzheimer's disease. Neurosci Lett. 1999;269:52–4. https://doi.org/10.1016/S0304-3940(99)00406-1.
53. Beasley AS, Anderson C, McArthur J, Sacktor N, Nath A, Cotter RJ. Characterization of Nitrotyrosine-Modified Proteins in Cerebrospinal Fluid. Clin Proteom. 2010;6:29–41. https://doi.org/10.1007/s12014-010-9041-4.

# Figures

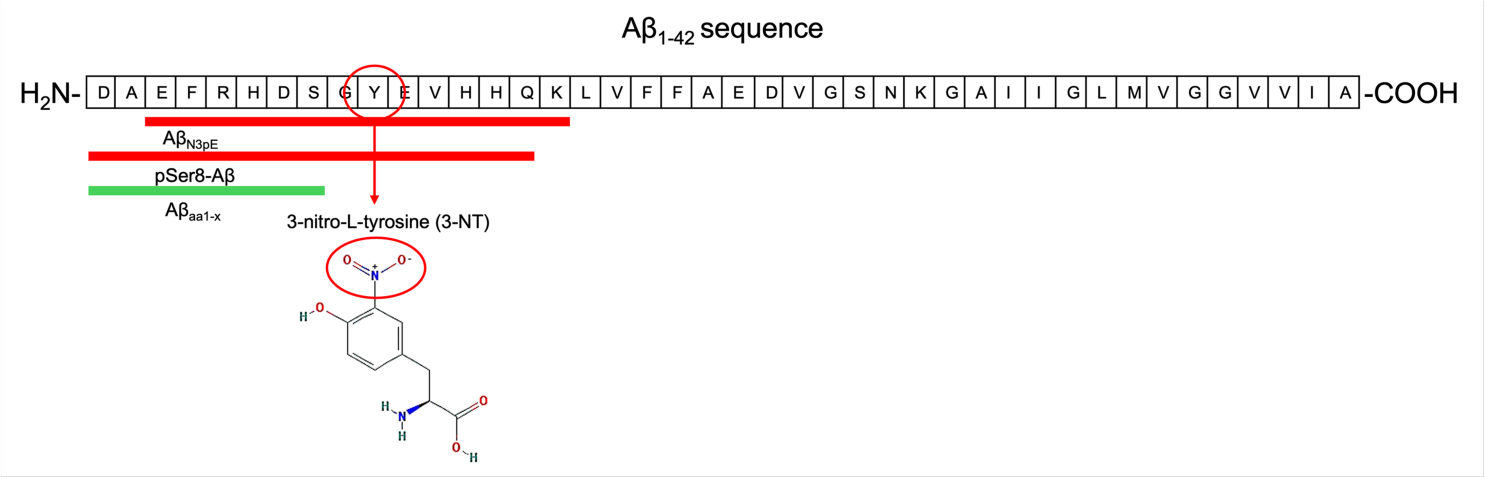
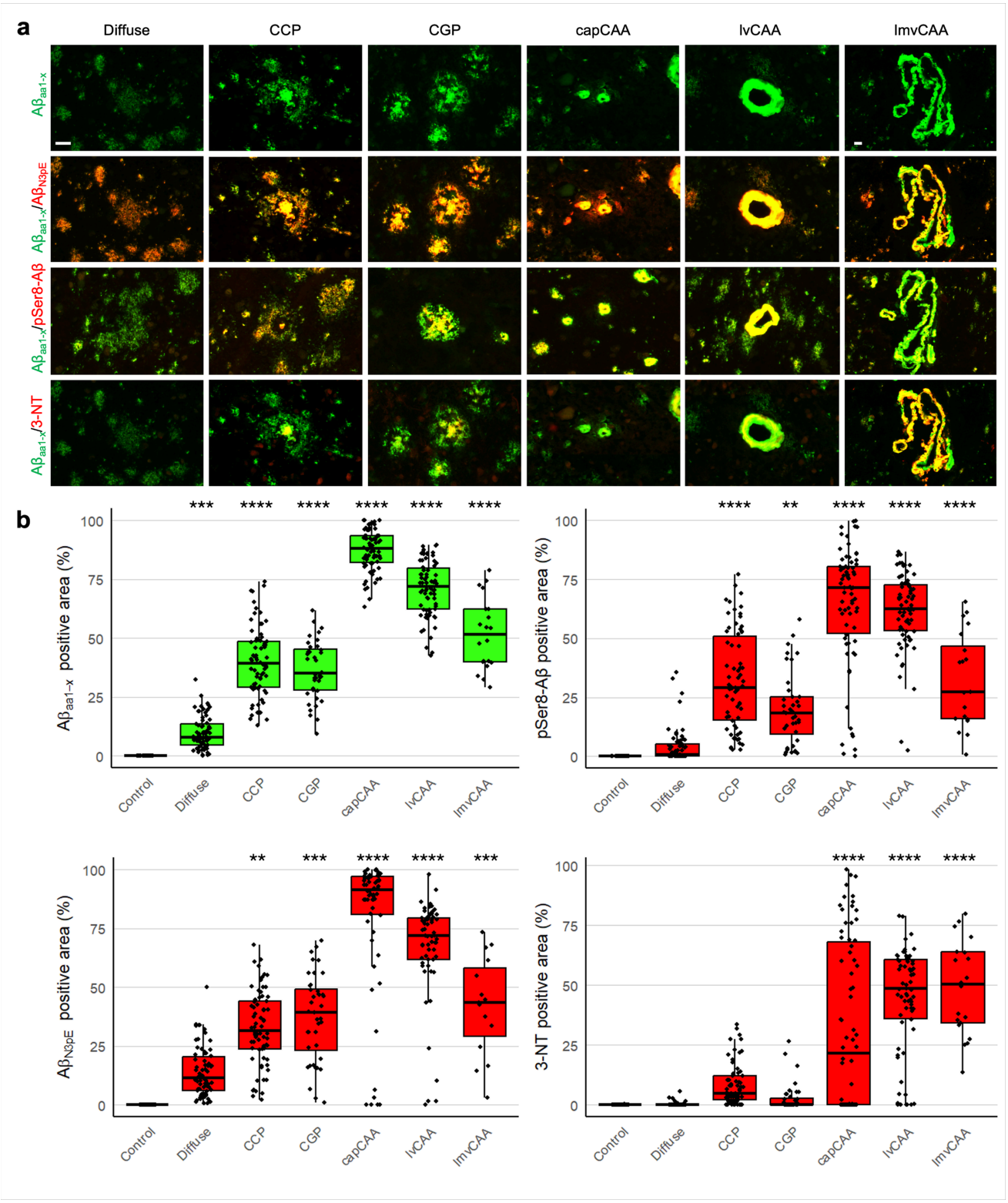



**Figure 1**

**Amino acid sequence of the $A\beta_{1-42}$ peptide.**

The epitopes recognized by the antibodies used for immunofluorescent staining, including $A\beta_{aa1-x}$, $A\beta_{N3pE}$, pSer8-Aβ, 3-NT are indicated below the sequence.

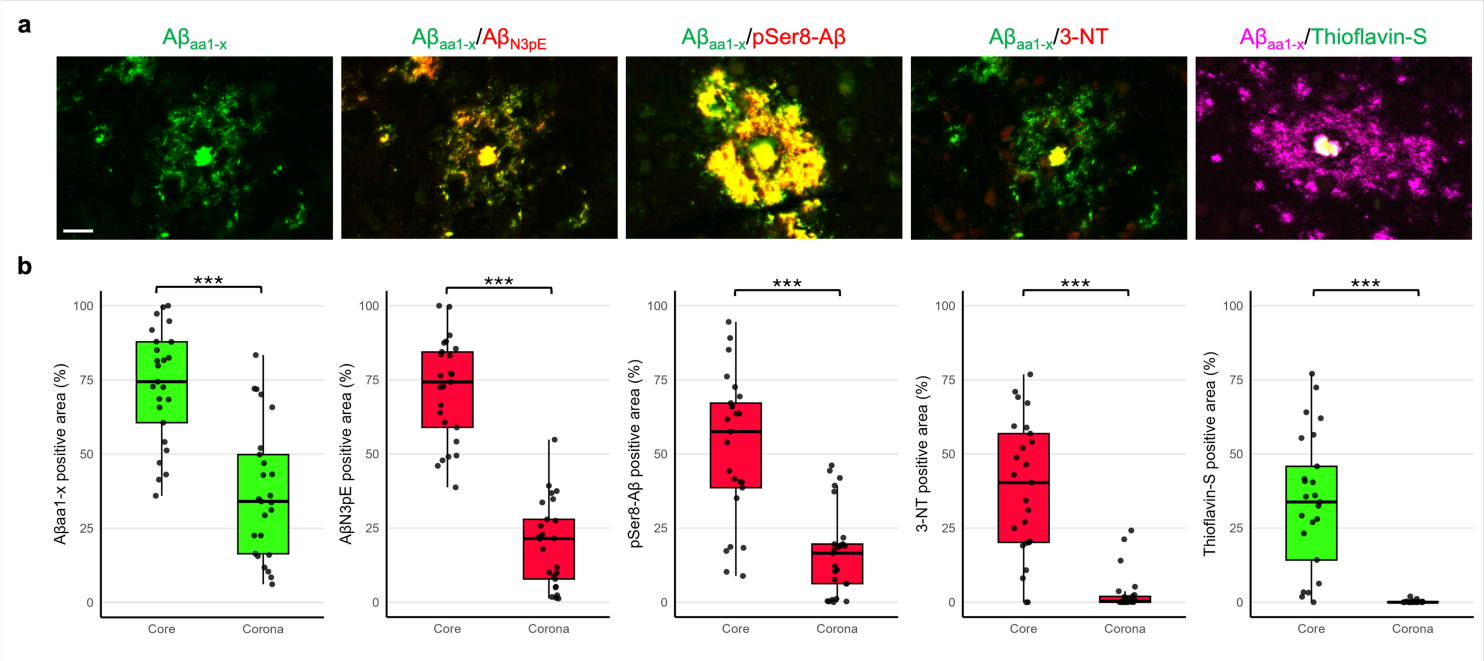



## Figure 2

**Quantification of Aβ species across distinct deposits.**

(a) Representative staining and (b) quantification of Aβ species ($Aβ_{aa1-x}$, $Aβ_{N3pE}$, pSer8-Aβ) and of 3-nitrotyrosine (3-NT) immunoreactivity, always overlapping with Aβ staining, using two triple-stain combinations: $Aβ_{aa1-x}$ + $Aβ_{N3pE}$ + 3-NT, and $Aβ_{aa1-x}$ + pSer8-Aβ + 3-NT, across distinct deposit groups. Signal is expressed as

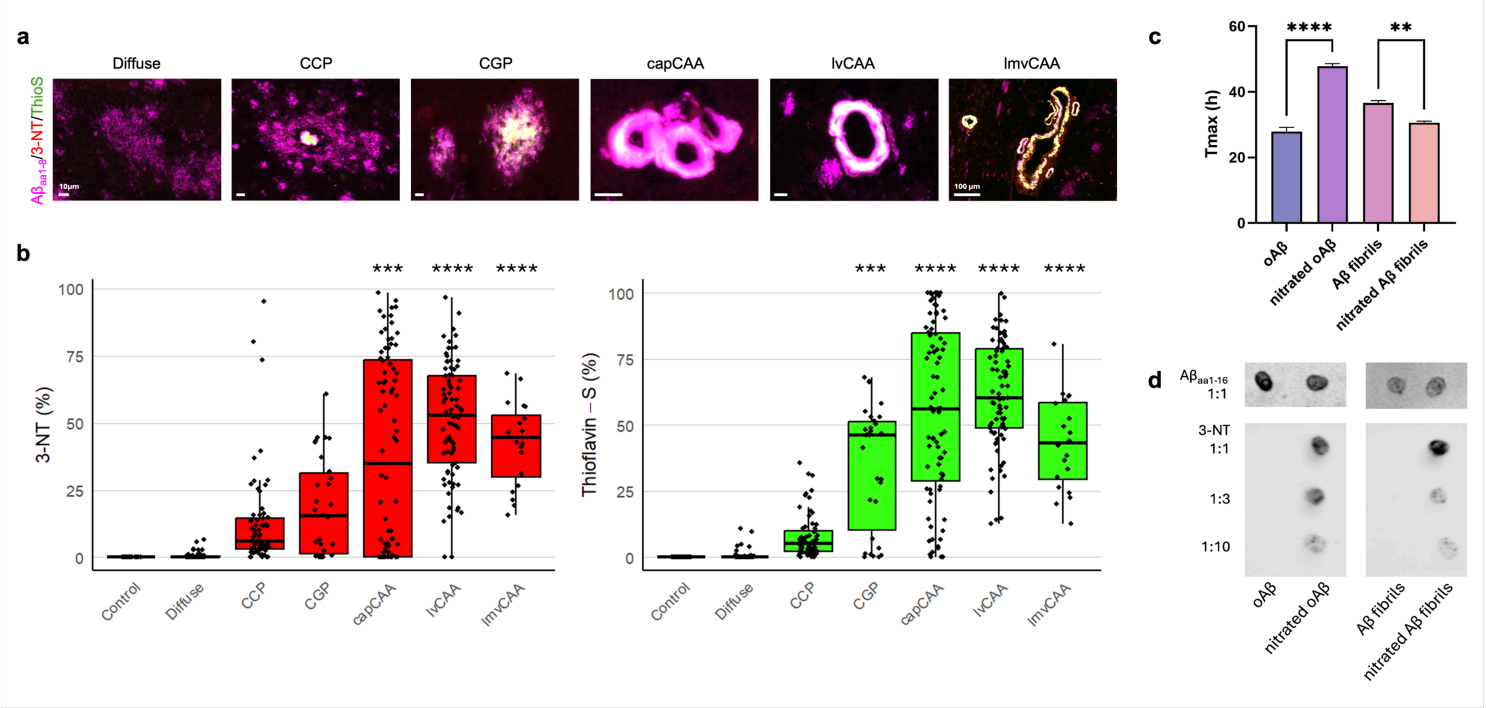
the percentage of the annotated deposit area occupied by pixels with fluorescence intensity above the predefined threshold (positive area [%]).Boxplots show median and interquartile range with each dot representing a single measurement within a subject (n=5-10 per subject). Pairwise comparisons were performed using linear mixed-effects models with subject as a random intercept; only comparisons versus controls are shown (**p<0.01, ***p<0.001, ****p<0.0001 after FDR correction). Full statistical results are provided in **Additional file 2**. Scale bar = 20 µm for all images; lmvCAA panels were acquired at a different magnification and therefore display an individual 20 µm scale bar. capCAA capillary CAA; lmvCAA leptomeningeal vessels CAA; lvCAA larger-vessel CAA; CCP classic cored plaques; CGP coarse-grained plaques.




## Figure 3

**Quantification of core versus corona in classic core plaques.**

(a) Representative images of $A\beta_{aa1\text{-}x}$, and of $A\beta_{N3pE}$, pSer8-Aβ, 3-NT and thioflavin-S overlapping with $A\beta_{aa1\text{-}x}$ staining in classic cored plaques. (b) Quantification of AβN3pE, pSer8-Aβ, 3-NT, and thioflavin-S immunoreactivity in the plaque core and corona. Signal is expressed as the percentage of the annotated core or corona area occupied by pixels with fluorescence intensity above the predefined threshold (positive area [%]). Boxplots show the median and interquartile range with whiskers extending to the minimum and maximum values. Each dot represents a single datapoint within a subject (n=5 per subject). To avoid inflating sample size, statistical analyses were performed on subject-level (n=5) using Mann-Whitney U test. ***p<0.001. Scalebar = 20 µm applies to all images.




## Figure 4

**Nitration is associated with β-pleated sheet conformation in Aβ deposits and influences aggregation kinetics.**

(a) Representative images showing $A\beta_{aa1\text{-}x}$/3-NT/thioflavin-S staining across distinct Aβ deposits. (b) Quantification of 3-NT and thioflavin-S staining. Signal is expressed as the percentage of the annotated deposit area occupied by pixels with fluorescence intensity above the predefined threshold (positive area [%]). Boxplots show median and interquartile range with each dot representing a single measurement within a subject (n=5-10 per subject). Pairwise comparisons were performed using linear mixed-effects models with subject as a random intercept; only comparisons versus controls are shown (***p<0.001, ****p<0.0001 after FDR correction). Full statistical results are provided in **Additional file 2**. (c) Thioflavin-T kinetic assay showing the time required for each assembly (pre-formed oligomers and fibrils, nitrated or not) to reach maximal fluorescence intensity. Bars represent means ± SEM of n=3 independent measures. **p<0.01, ****p<0.0001 by one-way ANOVA with Tukey's post-hoc test. (d) Representative dot blot confirming Aβ presence with the anti-Aβ 6E10 antibody (top inset) and nitration with anti-3-NT in pre-formed $A\beta_{1\text{-}42}$ oligomers and fibrils, either nitrated or not, at different dilutions. CAA cerebral amyloid angiopathy; (capCAA) capillary CAA; (CCP) classic cored plaques; (CGP) coarse-grained plaques; (lmvCAA) leptomeningeal vessel CAA; (lvCAA) larger-vessel CAA; (oAβ) $A\beta_{1\text{-}42}$ oligomers. Scale bar = 10 µm for all images except for lmvCAA, which was acquired at a different magnification and has its own 100 µm scale bar.

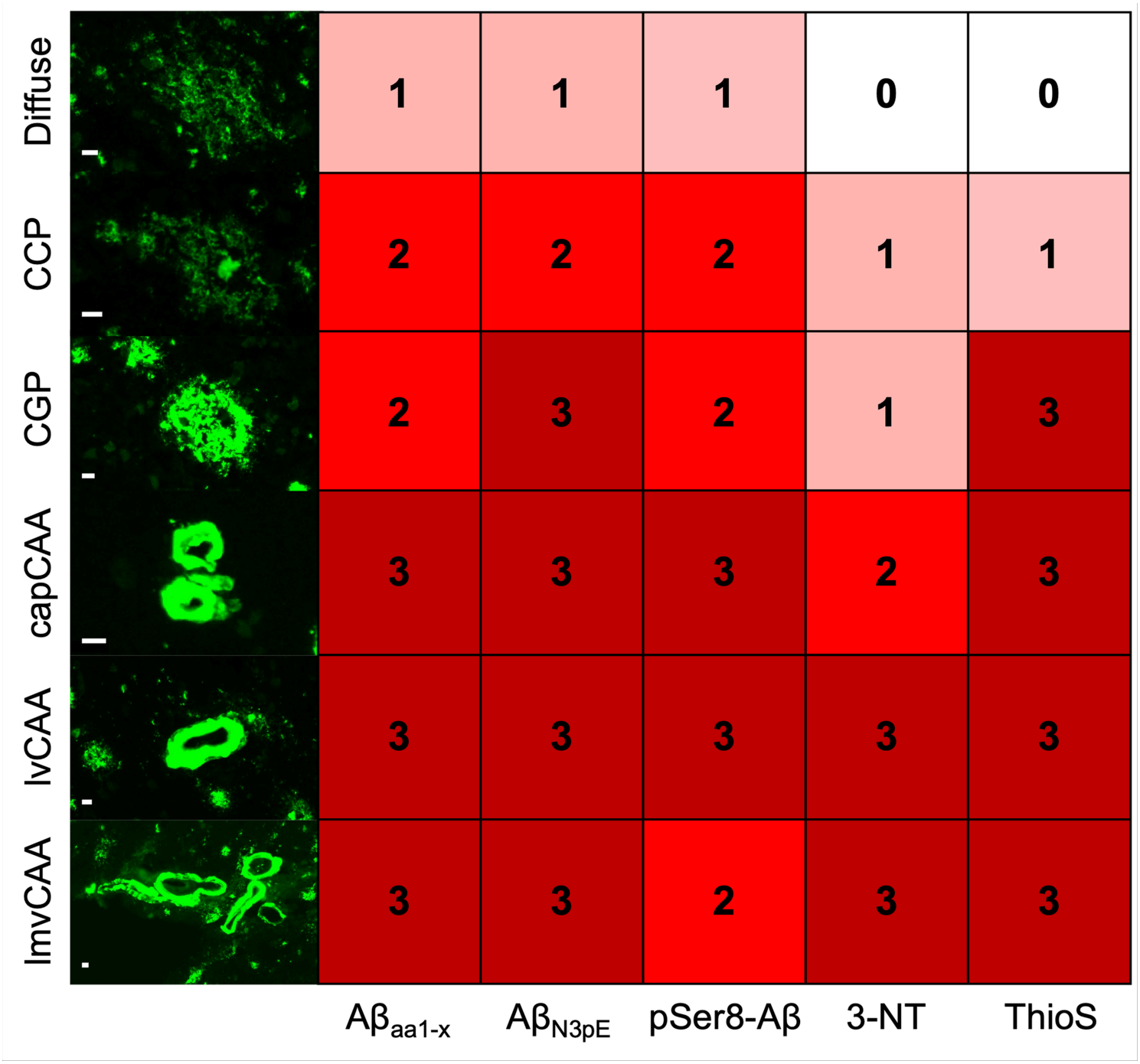
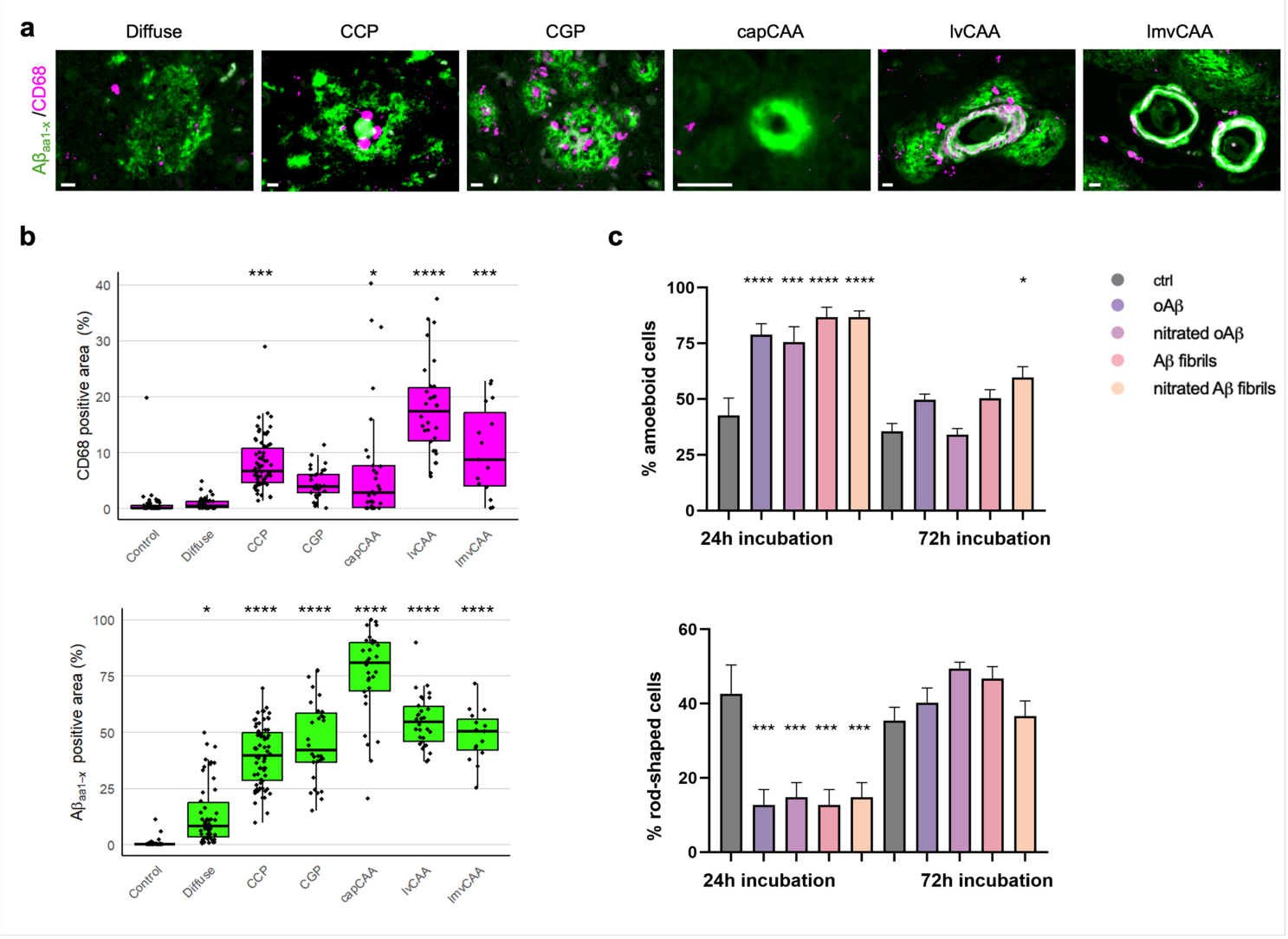



**Figure 5**

**Heatmap of Aβ species, nitration, and thioflavin-S positivity across distinct deposit types.**

Left panels display representative immunofluorescence images ($Aβ_{aa1-x}$ staining) illustrating the distinct deposit types. The right heatmap displays the relative burden of distinct Aβ species, nitration, and Thioflavin-S (ThioS) within each deposit type. To construct the heatmap, the relative percentage of positive pixels was calculated and categorized into a semi-quantitative ordinal scale: 0 (absent/no staining), 1 (mild), 2 (moderate), and 3 (maximal positivity). Abbreviations: CAA, cerebral amyloid angiopathy; capCAA, capillary CAA; CCP, classic cored plaque; CGP, coarse-grained plaque; lmvCAA, leptomeningeal vessel CAA; lvCAA, larger-vessel CAA. Scale bar = 10 μm.




## Figure 6

**Quantification of CD68+ microglia in Aβ deposits and in vitro**.

(a) Representative $Aβ_{aa1-x}$/CD68 staining of distinct Aβ deposit types. (b) Quantification of $Aβ_{aa1-x}$ and CD68 immunoreactivity. Signal is expressed as the percentage of the annotated deposit area occupied by pixels with fluorescence intensity above the predefined threshold (positive area [%]). Boxplots show median and interquartile range with each dot representing a single measurement within a subject (n=10 per subject). Pairwise comparisons were performed using linear mixed-effects models with subject as a random intercept; only comparisons versus controls are shown (*p<0.05, ***p<0.001, ****p<0.0001 after FDR correction). Full statistical results are provided in **Additional file 2**. (c) Morphological analysis of BV2 microglia cells treated with pre-formed $Aβ_{1-42}$ fibrils or oligomers (oAβ), nitrated or not. Datapoints represent the percentage of each morphology (amoeboid, rod-shaped and ramified morphologies) relative to total differentiated cells per well. Ramified morphologies, representing a resting phenotype, were excluded from quantitative analysis because they accounted for a negligible fraction of the overall differentiated population. Bars represent means ± SEM from three independent experiments with n=3-4 each. *p<0.05, ***p<0.001, ****p<0.0001 vs respective controls by one-way ANOVA with Tukey's post-hoc test. Controls (ctrl) showed no significant differences between 24 and 72 h for either phenotype. CAA cerebral amyloid angiopathy; capCAA capillary CAA; lmvCAA

leptomeningeal vessel CAA; lvCAA larger-vessel CAA; CCP classic cored plaque; CGP coarse-grained plaque. Scale bar = 10 μm.

## Supplementary Files

This is a list of supplementary files associated with this preprint. Click to download.

- BasileART2026Additionalfile1.docx
- BasileART2026Additionalfile2.xlsx
- BasileART2026Additionalfile3.tif